



RESEARCH ARTICLE | AUGUST 12 2024

Bandgap tuning in $\text{Zn}_x\text{Cd}_{1-x}\text{Te}$ superlattices through variable atomic ordering **FREE**


V. Barone ; R. J. Ellingson ; S. V. Khare





J. Chem. Phys. 161, 064703 (2024)


<https://doi.org/10.1063/5.0221674>




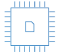
 Nanotechnology & Materials Science


 Optics & Photonics

 Impedance Analysis

 Scanning Probe Microscopy

 Sensors


 Failure Analysis & Semiconductors



Unlock the Full Spectrum. From DC to 8.5 GHz.

Your Application. Measured.

[Find out more](#)



Bandgap tuning in $\text{Zn}_x\text{Cd}_{1-x}\text{Te}$ superlattices through variable atomic ordering

Cite as: J. Chem. Phys. 161, 064703 (2024); doi: 10.1063/5.0221674

Submitted: 2 June 2024 • Accepted: 26 July 2024 •

Published Online: 12 August 2024



View Online



Export Citation



CrossMark

V. Barone,^{a)}  R. J. Ellingson,  and S. V. Khare

AFFILIATIONS

Department of Physics, Wright Center for Photovoltaics Innovation and Commercialization, University of Toledo, Toledo, Ohio 43606, USA

^{a)} Author to whom correspondence should be addressed: vbarone@rockets.utoledo.edu

ABSTRACT

We explore the entire search space of 32-layer $\text{Zn}_x\text{Cd}_{1-x}\text{Te}$ superlattices to find the structures that minimize and maximize the bandgap at each possible zinc concentration. The searching is accomplished through an accurate and efficient combination of valence force field dynamics, the empirical pseudopotential method, and the folded spectrum method. We also describe the use of an alternate preconditioner that improves the robustness and efficiency of the locally optimal preconditioned conjugate gradient's solutions to the folded spectrum method. The physical properties of these superlattices, such as their formation energies, bandgaps, densities of states, effective masses, and optical response functions, are investigated with density functional theory paired with hybrid functionals and compare well to available experimental measurements. It is revealed that the bandgap of $\text{Zn}_x\text{Cd}_{1-x}\text{Te}$ may change by up to 0.2 eV depending on how the layers in the superlattice are ordered. Stacking order has a large, irregular effect on the effective masses, but optical response functions seem insensitive to it.

Published under an exclusive license by AIP Publishing. <https://doi.org/10.1063/5.0221674>

I. INTRODUCTION

Semiconductor alloys are commonly employed for bandgap tuning.^{1–6} Variance in composition is the most common method of tuning in alloys, but commonly used growth techniques (molecular beam epitaxy^{7,8} or chemical vapor decomposition,^{9,10} for example) also allow selective deposition of specific atomic layers onto a growing crystal. Since optical properties of a material tend to be sensitive to the material's atomic structure, these methods may allow for further control of the bandgap, either replacing, or working alongside, standard composition variance.

The specification of atomic configurations to obtain a target material characteristic is known as an “inverse design problem.” Inverse design problems for the optimization of properties such as the bandgap value and transition type, Curie temperature, piezoelectric coefficients, and energetic stability have previously been solved.^{11–18} The methods of solving these problems depend heavily on the target application and available resources. This article focuses on the bandgaps of $\text{Zn}_x\text{Cd}_{1-x}\text{Te}$ layered alloys. This problem most closely resembles the one solved by Franceschetti and Zunger, and later Kim *et al.*,^{12,15} who used empirical methods to determine the maximum and minimum bandgap configurations of (Al, Ga)As superlattices.

This work considers $\text{Zn}_x\text{Cd}_{1-x}\text{Te}$ for its use in photovoltaic (PV) applications, although its wide bandgap and tellurium-rich composition also make it a common choice for use in radiation detection.^{19–21} For PV, according to the Shockley–Queisser limit,^{22,23} CdTe without zinc already has a nearly ideal bandgap (1.5 eV) for use in single junction cells. With the addition of zinc, the bandgap increases to over 2.0 eV, making $\text{Zn}_x\text{Cd}_{1-x}\text{Te}$ appropriate for tandem PV cells.^{24–29}

Other than the vast amount of experimental work on $\text{Zn}_x\text{Cd}_{1-x}\text{Te}$,^{24–30} there also exist many theoretical studies on the material.^{25,31–38} In all current theory to our knowledge, $\text{Zn}_x\text{Cd}_{1-x}\text{Te}$ is modeled as a random alloy, either by the virtual crystal approximation,^{25,33} special quasirandom structures,^{31,36} or consideration of some/all possible combinations of a small simulation cell.^{32,34,35} This is perhaps unsurprising, as the virtual crystal approximation in its general formulation represents a maximally random structure, and modern first-principles calculations even for cells with a “small” number of atoms can be prohibitively expensive. The study of ordered structures does not lend itself well to either method: the virtual crystal approximation is unable to differentiate between ordered structures, and first-principles techniques require the use of costly methods to accurately describe optoelectronic properties.^{39–46}

In this work, we study the optoelectronic properties of $\text{Zn}_x\text{Cd}_{1-x}\text{Te}$ ($0 \leq x \leq 1$) layered alloys $\approx 50 \text{ \AA}$ in height, corresponding to over 65 000 different models to consider. The cost of using *ab initio* methods for computing excited-state properties prohibits an accurate bandgap screening of these models. To this end, we first estimate the ground-state atomic positions with a semiempirical valence force-field model.⁴⁷ We then use the empirical pseudopotential method (EPM), paired with a fast and accurate solution to the single-particle Schrödinger equation,^{48,49} to quickly determine which structures at a given zinc concentration maximize and minimize the bandgap. Density functional theory (DFT) calculations are then employed to study the physical properties of these structures. Combining the EPM and DFT provides high-quality predictions for only a select few $\text{Zn}_x\text{Cd}_{1-x}\text{Te}$ structures of interest, which would not be possible by using either the EPM or DFT alone.

Specifics of the EPM, DFT, and bandgap screening procedures are given in Sec. II. Our improvements to the convergence of the EPM, as well as the physical properties of select $\text{Zn}_x\text{Cd}_{1-x}\text{Te}$ structures, are detailed in Sec. III. Finally, in Sec. IV, we summarize our findings.

II. METHODS

For clarity, we now briefly outline the chronological series of steps taken to reach the results presented in Sec. III. Details of each step can be found within this section. First, a DFT molecular dynamics (MD) calculation was performed on $\text{Zn}_{0.5}\text{Cd}_{0.5}\text{Te}$ to obtain atomic forces. Second, Keating force-field parameters were obtained from the MD run.⁴⁷ Third, the potential for the empirical pseudopotentials was fit to existing bands from the literature.^{50,51} Fourth, all possible permutations of 32-layer $\text{Zn}_x\text{Cd}_{1-x}\text{Te}$ were generated and relaxed with the Keating potential. The folded spectrum method (FSM)^{48,49} was combined with the EPM to calculate the bandgap of each structure. Fifth, the structures with the minimum and maximum bandgaps, as predicted by step 4, had basic DFT calculations performed on them at the generalized gradient approximation (GGA) level. Sixth, high quality DFT calculations were performed on the minimum and maximum bandgap structures at $x = 0.00, 0.25, 0.50, 0.75, 1.00$.

A. Density functional theory

We use the Vienna *Ab initio* Simulation Package (VASP version 6.1.0⁵²⁻⁵⁴) for all DFT calculations. Standard PAW potentials are used to represent the core electrons,^{55,56} $3d^{10}4s^2, 4s^25s^2$, and $5s^25p^4$ valence electrons were included for zinc, cadmium, and tellurium, respectively. For MD, structural relaxations, and effective masses, we treat exchange–correlation effects with the semi-local Perdew–Burke–Ernzerhof (PBE) functional.⁵⁷ All other calculations employ the Heyd–Scuseria–Ernzerhof hybrid functional with the screening parameter set to 0.2 \AA^{-1} (HSE06)⁵⁸ for the exchange–correlation effects.

The MD calculation responsible for the Keating force field parameters used a plane wave cutoff equivalent to 280 eV, a $5 \times 5 \times 5$ mesh of k -points for integrations, and Gaussian smearing with a width of 0.04 eV to set partial occupancies. The MD itself ran for 20 ps at 100 K (2 fs time step). We also tested an MD at 300 K, but the

difference between DFT forces and Keating forces was more acceptable for the MD at 100 K. For structural relaxations of the 32-layer $\text{Zn}_x\text{Cd}_{1-x}\text{Te}$ cell, the plane wave basis cutoff energy is increased to 370 eV, a $5 \times 5 \times 1$ mesh of k -points is used, and partial occupancies are set as they were in the MD calculations. The increased cutoff energy is to ensure that Pulay stress is correctly treated. Both atoms and the cell shape are adjusted until the force on any given atom is less than 0.01 eV/\AA .

Bandgaps, crystal orbital Hamilton populations (COHPs), densities of states (DOS), and the dielectric response functions are calculated with HSE06. For these calculations, the plane wave cutoff energy is set to 280 eV, a $3 \times 3 \times 1$ k -point grid is used, and tetrahedron smearing with Blöchl corrections⁵⁹ is employed for partial occupancies. For analysis of the COHPs, we use Local Orbital Basis Suite Toward Electronic-Structure Reconstruction (LOBSTER version 4.0.0⁶⁰⁻⁶⁵). The basis set for projections is the LOBSTER default and results in a charge spilling of 1.2% at most. The dielectric functions are calculated according to the independent particle approximation described by Gajdoš *et al.*⁶⁶ and implemented in the VASP. Specifically, the imaginary portion of the dielectric function ϵ_2 , as a function of energy E , is calculated through

$$\epsilon_{2,ij}(E) = \frac{4\pi^2 e^2}{\Omega} \lim_{q \rightarrow 0} \frac{1}{q} \sum_{v,c,\mathbf{k}} w_{\mathbf{k}} \delta(\epsilon_c(\mathbf{k}) - \epsilon_v(\mathbf{k}) - E) \times \langle u_{c,\mathbf{k}+\hat{i}\mathbf{q}} | u_{v,\mathbf{k}} \rangle \langle u_{v,\mathbf{k}} | u_{c,\mathbf{k}+\hat{j}\mathbf{q}} \rangle, \quad (1)$$

where v and c enumerate the valence and conduction bands and the functions $|u_{b,\mathbf{k}}\rangle$ are the cell periodic parts of the wavefunctions at k -point \mathbf{k} . The real part of the dielectric function, ϵ_1 , is solved using the Kramers–Kronig principal value integral,

$$\epsilon_{1,ij}(E) = 1 + \frac{2}{\pi} \int_0^\infty \frac{x \epsilon_{2,ij}(x)}{x^2 - E^2} dx. \quad (2)$$

The absorption coefficient α and the reflectivity R are calculated as⁶⁷

$$\alpha(E) = \frac{2}{\hbar c} E \kappa, \quad (3)$$

$$R(E) = \frac{(\eta - 1)^2 + \kappa^2}{(\eta + 1)^2 + \kappa^2}, \quad (4)$$

where the complex refractive index $\eta + i\kappa$ is defined as

$$\eta(E) = \frac{1}{\sqrt{2}} \left[+\epsilon_1 + (\epsilon_1^2 + \epsilon_2^2)^{1/2} \right]^{1/2}, \quad (5)$$

$$\kappa(E) = \frac{1}{\sqrt{2}} \left[-\epsilon_1 + (\epsilon_1^2 + \epsilon_2^2)^{1/2} \right]^{1/2}. \quad (6)$$

The total number of bands calculated was increased to 600 for the convergence of the optical response functions, and the principle value integral was solved using a complex shift value of 0.1 eV for the denominator.

B. Empirical pseudopotential, folded spectrum methods

We employ the EPM for initial exploration of all possible $\text{Zn}_x\text{Cd}_{1-x}\text{Te}$ structures due to its combination of accuracy, efficiency, and non-reliance on self-consistency (necessary for the FSM

described below). The merits, drawbacks, and theory of the EPM are described by Cohen and Heine.⁶⁸ In summary, the single-particle energies E and wavefunctions ψ of a system are found by solving

$$\hat{H}\psi = (\hat{T} + \hat{V})\psi = E\psi, \quad (7)$$

where \hat{T} and \hat{V} are the kinetic and potential energy operators of the Hamiltonian \hat{H} . Usually, $\hat{T} = \hbar^2/(2m_0)\nabla^2$ and nonlocality is included within \hat{V} . An alternative way of including nonlocality was suggested by Chelikowsky *et al.*⁶⁹ in which $\hat{T} \rightarrow \hat{T}'$ by replacing m_0 by an adjustable “effective mass”: $\hat{T}' = \hbar^2/(2m^*)\nabla^2$. We will use the \hat{T}' notation to avoid confusion with effective masses later reported in this work. Other than simplicity, this method has the important result that \hat{V} may remain a purely local function, allowing it to be written as the sum of atomic pseudopotentials v ,

$$\hat{V} = \frac{1}{N} \sum_j S_j v_j(|\mathbf{G} - \mathbf{G}'|), \quad (8)$$

where N is the number of atoms, S_j is the structure factor for species j , and \mathbf{G} are reciprocal lattice vectors. Although v is only sampled at specific values related to the dimensions of the lattice, it is in theory defined for any point in reciprocal space q . Our choice of $v(q)$ is detailed in Appendix B. The purely local \hat{V} allows the action $\hat{H}\psi$ to be computed as a convolution instead of a full matrix multiplication,^{70,71} which is necessary for the efficiency of the method.

We also use the FSM,^{48,49} which allows the calculation of electronic states arbitrarily deep within \hat{H} without the need to solve for lower energy states. It works by “folding” the (eigenvalue) spectrum of \hat{H} about a reference energy E_{ref} , transforming the single particle Schrödinger equation into

$$(\hat{H} - E_{\text{ref}})^2 \psi = (E - E_{\text{ref}})^2 \psi = E' \psi. \quad (9)$$

The eigenvalues of $(\hat{H} - E_{\text{ref}})^2$, E' , are related to the eigenvalues of interest, E , by $E' = (E - E_{\text{ref}})^2$. The benefit of the FSM is that solving for the lowest few E' (an easy job for iterative eigensolvers) yields the few E closest to E_{ref} (a difficult job for iterative eigensolvers). By choosing E_{ref} correctly, the FSM can report the bandgap by converging only two electronic bands, independent of the size of the structure.

An alternative to the FSM would be to solve for all the valence bands plus one conduction band for each structure to get the bandgap energies. In the present case of 32-layer $\text{Zn}_x\text{Cd}_{1-x}\text{Te}$, this would involve converging 100 and 29 bands per k -point instead of two. The former method is about 20 times slower than the latter in our implementation—see Sec. III A for further discussion.

C. Bandgap screening of $\text{Zn}_x\text{Cd}_{1-x}\text{Te}$

Both the Keating force field and EPM parameters are fit using particle swarm optimization (PSO), a global optimization algorithm.⁷² The PSO involves hyperparameters for particle inertia, individual particle strength, and global particle strength. We choose 0.5, 1.0, and 1.0 for each of these hyperparameters, respectively.

For the Keating potential, we compare the atomic forces from 1000 equispaced configurations (out of 10 000 total) from a DFT MD

run on $\text{Zn}_{0.5}\text{Cd}_{0.5}\text{Te}$ to the atomic forces from the Keating potential applied to the same configurations. PSO is used to adjust α_{ij} s and β_{ij} s in order to minimize the average error between the atomic forces from DFT and the atomic forces from the Keating potential. The optimized Keating potential parameters are given in Tables SI and SII of the [supplementary material](#). The predicted bond lengths for ZnTe (2.65 Å) and CdTe (2.80 Å) compare well with experiment^{73,74} and previous bond order potential parameterizations.^{37,38} Atomic movements in the present superlattices are expected to be constrained in such a way that the Keating model gives a sufficient description of the forces. This is supported by DFT calculations on the structures that minimize and maximize the bandgap: starting from initial crystallographic atomic positions, atoms were only 0.2 Å away from their minimum energy positions on average. For studies involving defects, surfaces, alloys, and other more complicated geometries, more sophisticated force field models^{37,38} should be used instead.

For the EPM parameters, we compare the band energies at a few special k -points [$L = (1/2, 1/2, 1/2)$, $\Gamma = (0, 0, 0)$, $X = (0, 1/2, 1/2)$, $U = (1/4, 5/8, 5/8)$, and $K = (3/8, 3/8, 3/4)$] between the reference data^{50,51} and the energies as calculated by the EPM. PSO is used to adjust the EPM parameters until a weighted average error between reference bands and EPM bands is minimized. As we are only interested in an accurate description of the bandgap, the weights are such that a few bands closest to the valence band maximum (VBM) and conduction band minimum (CBM) are more important than any other bands. The initial guesses for the EPM parameters were found by existing fits to zinc, cadmium, and tellurium from Cohen and Heine⁶⁸ before being adjusted by the PSO. To treat charge transfer, we fit two separate tellurium potentials: one for tellurium in ZnTe (notated $v_{\text{Te}[\text{ZnTe}]}$) and the other for tellurium in CdTe (notated $v_{\text{Te}[\text{CdTe}]}$). The actual tellurium potential used in the EPM depends on its immediate local environment. Te has four nearest neighbors, of which N_{Zn} are zinc and N_{Cd} are cadmium. The atomic potential given to tellurium in the EPM is

$$v_{\text{Te}} = \frac{N_{\text{Zn}}}{4} v_{\text{Te}[\text{ZnTe}]} + \frac{N_{\text{Cd}}}{4} v_{\text{Te}[\text{CdTe}]}. \quad (10)$$

This same method was previously used by Mäder and Zunger and Kim *et al.* for (Al, Ga)As.^{15,75} The optimized EPM parameters are given in Table I, and a plot of the atomic pseudopotentials is shown in Fig. 1.

With the Keating potential and EPM parameter fit, we predict the bandgap of each possible structure for $0 \leq x \leq 1$ in steps of 1/16. There are 2^{16} possible structures for our 32-layer $\text{Zn}_x\text{Cd}_{1-x}\text{Te}$ material since half of the layers are tellurium, which is never swapped for a different element. For each structure, we first relax the atoms using the Keating force field model and quenched Verlet integration.⁷⁶ The relaxation is performed until the force on any atom is less than 0.05 eV/Å. After relaxation, the FSM is applied with a basis set cutoff energy equivalent to 110 eV (over three times the maximum Fermi momentum of zinc, cadmium, or tellurium, as suggested by Cohen and Heine⁶⁸) on a $3 \times 3 \times 1$ k -point mesh. The FSM is converged to 0.1 meV, meaning that the VBM and CBM are converged to 0.01 eV.

In principle, one could determine the bandgap by carefully choosing E_{ref} to be in the middle of the gap and solving for two

TABLE I. EPM parameters used in this study. Te[ZnTe] is the result of fitting tellurium to the ZnTe reference data from Bernard and Zunger.⁵⁰ Te[CdTe] is the result of fitting tellurium to the CdTe reference data from Chelikowsky and Cohen.⁵¹ The actual potential used for tellurium is given by Eq. (10). The window length l and cutoff function Θ are defined in Appendix B and are identical for all elements: $l = 0.2 \text{ \AA}^{-1}$, $r = 1.5$, and $f = 0.75$.

| Element | T' (eV \AA^2) | ν_0 (eV) | ν_m (eV) | q_0 (\AA^{-1}) | q_m (\AA^{-1}) | q_c (\AA^{-1}) | s (\AA) | n |
|----------|---------------------------|--------------|--------------|-----------------------------|-----------------------------|-----------------------------|----------------------|-----------|
| Zn | 4.627 460 | -6.306 401 | 1.750 276 | 2.650 095 | 3.447 664 | 4.86 | 0.299 923 | 0.956 664 |
| Te[ZnTe] | 4.627 460 | -7.669 856 | 0.563 728 | 2.811 029 | 3.753 352 | 5.37 | 0.211 335 | 0.850 656 |
| Cd | 4.526 188 | -4.994 802 | 1.550 105 | 2.449 964 | 3.338 316 | 4.34 | 0.049 941 | 1.041 400 |
| Te[CdTe] | 4.526 188 | -7.702 521 | 0.263 247 | 2.944 099 | 3.783 317 | 5.37 | 0.062 864 | 1.057 374 |

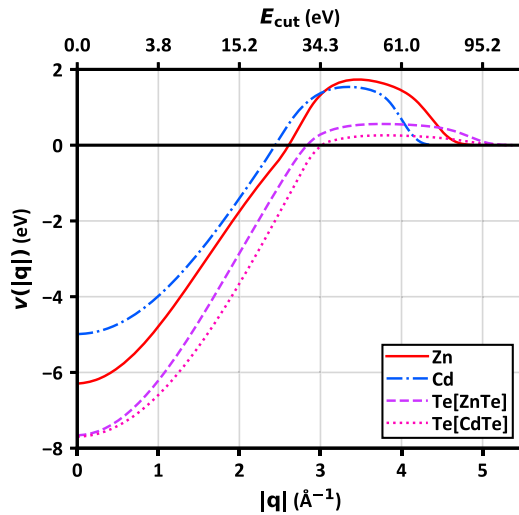


FIG. 1. Plots of the empirical pseudopotentials used in this work. Also included are the effective cutoff energies at each q point, defined through $E = \hbar^2/(2m)q^2$. Te[ZnTe] is the result of fitting tellurium to the ZnTe reference data from Bernard and Zunger.⁵⁰ Te[CdTe] is the result of fitting tellurium to the CdTe reference data from Chelikowsky and Cohen.⁵¹ The actual potential used for tellurium is given by Eq. (10).

bands. In practice, we have chosen to keep track of two reference energies—one for the valence bands ($E_{\text{ref,vb}}$) and the other for the conduction bands ($E_{\text{ref,cb}}$)—and using each to solve for a single band energy. Although the former is more efficient, it has the possibility of converging, say, two valence bands instead of one valence band and one conduction band. The latter method is easier to automate so long as the band edges are not heavily affected by atomic layer swaps.

The reference energies are initialized with a non-FSM calculation of a small $\text{Zn}_x\text{Cd}_{1-x}\text{Te}$ cell (for example, ZnTe, representable with only two atoms). They are then iteratively updated before each new FSM calculation. Specifically, E_{ref} at step $j + 1$ is calculated from the VBM and CBM of step j according to

$$E_{\text{ref,vb}}^{j+1} = \text{VBM}^j + \frac{1}{4}(\text{CBM}^j - \text{VBM}^j), \quad (11)$$

$$E_{\text{ref,cb}}^{j+1} = \text{CBM}^j - \frac{1}{4}(\text{CBM}^j - \text{VBM}^j). \quad (12)$$

By arranging the atomic layer swaps such that configuration $j + 1$ is similar to configuration j , this method ensures that the reference energies always remain close to their respective band edges. We occasionally did a non-FSM calculation to verify that the E_{ref} estimates were still correct.

III. DISCUSSION AND RESULTS

A. Convergence behavior of the folded spectrum method

We first discuss the convergence of the FSM, shown in Fig. 2, which shows the behavior of two different preconditioners in converging to the VBM and CBM of a CdTe cell of increasing size. Each data point is the average of five independent runs. The solution to Eq. (9) is solved via the Locally Optimal Block Preconditioned Conjugate Gradient (LOBPCG) method;^{78,79} thus, all further discussion technically only pertains to it. Preconditioner a refers to that first described by Teter *et al.*⁷⁷ and takes the form $\mathbf{K}_{\text{GG}'}^a = \delta_{\text{GG}'} (27 + 18x + 12x^2 + 8x^3)/(27 + 18x + 12x^2 + 8x^3 + 16x^4)$ with \mathbf{K} representing the preconditioner, \mathbf{G} representing a reciprocal lattice vector, and x being the ratio of the kinetic energy at some \mathbf{G} to the sum of the kinetic energies. For the FSM, the kinetic energy in preconditioner a must be scaled by E_{ref} —see Sec. SI of the [supplementary material](#). Preconditioner b is that given by Wang *et al.* and Canning *et al.*,^{48,49} designed for the FSM. It is (in standard units) $\mathbf{K}_{\text{GG}'}^b = \delta_{\text{GG}'} T_{\text{avg}}^2 / ((\hbar^2/(2m)|\mathbf{G}|^2 + V_{\text{avg}} - E_{\text{ref}})^2 + T_{\text{avg}}^2)$, with V_{avg} being the average potential and T_{avg} being the average kinetic energies.

In general, from Fig. 2(a), the number of steps required to converge the FSM are on the order of 100, significantly higher than the number of steps needed in the convergence of Hamiltonians without the use of the FSM, which is generally of order 10. This result is due to the fact that squaring the Hamiltonian increases its condition number by an order of magnitude, and the steps to converge conjugate gradient methods scale with the condition number.⁸⁰ This result was reported by Wang and Zunger,⁴⁸ who also note that the speed at which each FSM step can be completed more than makes up for the increase in the total number of FSM steps compared to solving the usual single particle Schrödinger equation.

Figure 2(a) also shows that the VBM requires more steps to converge than the CBM does. This is due to the fact that CdTe's topmost valence bands are triply degenerate at the Γ point when electron spin is not taken into account. Degenerate eigenvalues can slow the convergence of iterative eigensolvers, LOBPCG being one such example.^{78,79} Meanwhile, the CBM has no such degeneracy.

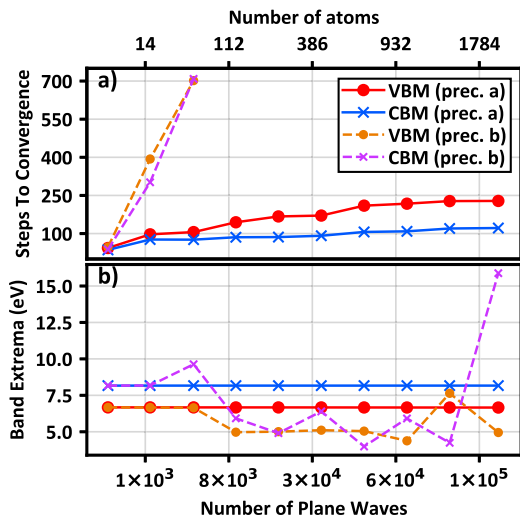


FIG. 2. Behavior of two preconditioners (prec.) for finding the band edges of differently sized CdTe cells using the FSM. Results are the average of five independent runs. Prec. *a*⁷⁷ (solid lines) performs better than prec. *b*^{48,49} (dashed lines), for both the valence (circles) and conduction (crosses) bands, although prec. *b* was designed for use with the FSM. In (a), the steps to convergence for prec. *b* are only plotted up to 3931 plane waves since prec. *b* converges to the incorrect results after this point, as is shown in (b).

The most surprising feature of Fig. 2 is the fact that preconditioner *a* outperforms preconditioner *b* (simply referred to as *a* and *b* for the remainder of this section) in terms of both steps to convergence and overall ability to converge to the correct band energies. In Fig. 2(a), *b*'s steps to convergence are only given up to 54 atoms (3931 plane waves) since after that point, *b* fails to consistently yield the correct VBM and CBM, as shown in Fig. 2(b). Even so, it is clear that *b* tends to converge slower than *a*—for a 16 atom supercell, *b* converges to the VBM and CBM in 393 and 302 steps, on average, respectively. *a* does the same in 97 and 77 steps. The more important issue is that *b* does not cause LOBPCG + FSM to give the correct bandgap for supercells greater than 54 atoms large and is thus unreliable for our needs in this work. *b* predicts the VBM to be between 2.4 and 14.5 eV and the CBM to be between 2.2 and 15.9 eV. *a* predicts the VBM and CBM consistently as 6.7 and 8.2 eV, respectively.

The failure of *b* is likely due to the small subspace associated with LOBPCG when only solving for one eigenvalue (size 3). To our knowledge, LOBPCG has only been paired with the FSM once before, in a study of CdSe nanoparticles by Tomo *et al.*⁸¹ This study tested the FSM with both *b* and no preconditioner for problems of up to 1061 atoms (141 625 plane waves), but reported LOBPCG + FSM to yield consistent band energies. They, however, were solving for ten band energies at once, with a subspace size of at least 30. When we increase the block size, we also see more consistent band energies with *b*, although this significantly increases the cost of finding the VBM and CBM. Other attempts to alter the LOBPCG routine (more aggressive orthonormalization, adjustment of T_{avg} as suggested by Wang and Zunger⁴⁸) were ineffective. The increased subspace size seems to remedy *b*'s inability to give correct band energies, but it does not meaningfully improve its rate of convergence compared to

a. For example, *a* finds the ten bands nearest to the VBM and CBM about ten times faster than *b* does for a 250 atom CdTe supercell.

B. Bandgap screening

The main results of the EPM exploration of 32-layer $\text{Zn}_x\text{Cd}_{1-x}\text{Te}$ are presented in Fig. 3(a) and Table II. Figure 3(a) shows the minima, maxima, and average bandgaps (BGs) of all possible 32-layer $\text{Zn}_x\text{Cd}_{1-x}\text{Te}$ models as predicted by the EPM. The orange shaded region indicates the full range of BGs, and the black bars at each x are violin plots indicating the distribution of BGs (the width of the violin plot correlates with the density of points). The “configuration” column of Table II gives the arrangement of zinc and cadmium atoms corresponding to the minimum and maximum BG configurations. We performed DFT (GGA) calculations on each of the minimum and maximum gap configurations, of which the BGs are shown in Fig. 3(b). We have no information on the GGA BG distribution of all 2^{16} structures, as obtaining this information would be too costly—we would not need the EPM otherwise. The lattice constant and formation energy columns of Table II also correspond to these DFT calculations.

From Fig. 3(a), the EPM predicts the BGs of the end members CdTe and ZnTe to be 1.5 and 2.0 eV, respectively, in excellent agreement with experimental data.^{25–28} This agreement is not surprising, however, as the EPM was fit to experimental data. For the layered superlattices, their BGs are reported to vary by about 0.2 eV at most, with the most variance for $x \approx 0.5$. Figure 3(b) exhibits the well-known “bandgap problem,”⁴⁴ where the DFT GGA results underestimate the BG by about 0.9 eV. A constant shift of the conduction bands by 0.9 eV would alter the GGA estimations of BG

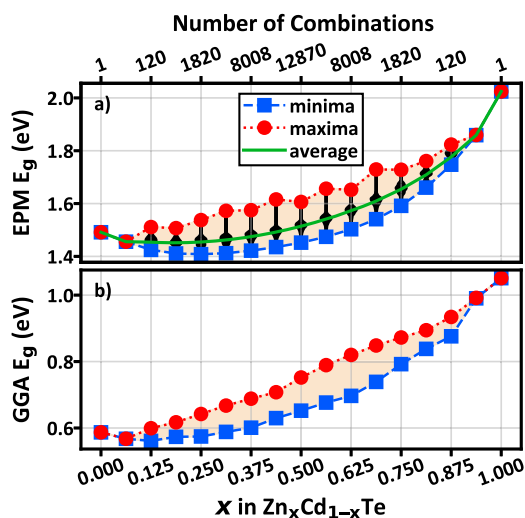


FIG. 3. (a) Bandgaps for each possible 32-layer $\text{Zn}_x\text{Cd}_{1-x}\text{Te}$ supercell (65 536 total possibilities) predicted by the EPM. The range of all possible bandgaps is represented by the orange shaded area, and the minima, maxima, and average bandgaps are shown directly. The distribution of the remaining bandgaps is indicated by the widths of the black marks at each x (wider = higher density of configurations with a given bandgap). (b) Similar to (a), but only the minimum and maximum bandgaps (as estimated by the EPM) are calculated with GGA. No information on the distribution of all 65 536 GGA gaps is available.

TABLE II. Summary of 30 DFT GGA calculations on the minimum and maximum bandgap configurations of $\text{Zn}_x\text{Cd}_{1-x}\text{Te}$. For each x , the 16-cation-layer configuration yielding the minimum and maximum bandgaps is given along with the calculated lattice constants a and formation energies E_f . Configurations are interpreted as layers stacked in the c direction of the crystal, where “Z” and “C” indicate the layers of zinc and cadmium atoms, respectively. Te layers are not indicated, as they are the same for all layers.

| x | Minimum gap | | | Maximum gap | | |
|--------|------------------|---------|------------------|------------------|---------|------------------|
| | Configuration | a (Å) | E_f (meV/f.u.) | Configuration | a (Å) | E_f (meV/f.u.) |
| 0.0000 | CCCCCCCCCCCCCCCC | 6.61 | −923 | ... | ... | ... |
| 0.0625 | ZCCCCCCCCCCCCCCC | 6.61 | −920 | ... | ... | ... |
| 0.1250 | ZZCCCCCCCCCCCCC | 6.59 | −915 | CCZCCCCCCCCCZCCC | 6.57 | −916 |
| 0.1875 | ZZZCCCCCCCCCCCC | 6.57 | −912 | CCCCCZCCCCCZZ | 6.54 | −913 |
| 0.2500 | ZZZZCCCCCCCCCCC | 6.55 | −908 | ZCCCCZCCCCZCCC | 6.51 | −909 |
| 0.3125 | ZCZZZCCCCCCCCC | 6.52 | −906 | CCCZCCZCCZCCCZ | 6.47 | −908 |
| 0.3750 | ZZZZCZCCCCCCCC | 6.50 | −905 | ZCZCCZCCZCCZCC | 6.45 | −907 |
| 0.4375 | ZZZZZZCCCCCCCC | 6.47 | −905 | ZCZCZCCZCCZCCZC | 6.42 | −907 |
| 0.5000 | ZZZZZZZCCCCCCC | 6.44 | −906 | ZCZZCZCCZCZCCCZ | 6.39 | −907 |
| 0.5625 | ZZZZZZZZCCCCCC | 6.41 | −908 | CCZZCCZZCCZZCZ | 6.36 | −909 |
| 0.6250 | ZZZZZZZZZCCCCC | 6.38 | −910 | CZZCCZCZZCZZZ | 6.33 | −911 |
| 0.6875 | ZZZZZZZZZZCCCC | 6.34 | −913 | ZCZZZCCZZCZZZ | 6.31 | −914 |
| 0.7500 | ZZZZZZZZZZZCCC | 6.31 | −917 | ZZCCZZZCZCZZZZ | 6.29 | −918 |
| 0.8125 | ZZZZZZZZZZZZCCC | 6.29 | −921 | ZZCZZZZZCZZCZZ | 6.26 | −921 |
| 0.8750 | ZZZZZZZZZZZZCZC | 6.27 | −925 | ZZZZCZZZZZZZZC | 6.24 | −927 |
| 0.9375 | ZZZZZZZZZZZZZZC | 6.22 | −932 | ... | ... | ... |
| 1.0000 | ZZZZZZZZZZZZZZZ | 6.19 | −938 | ... | ... | ... |

TABLE III. Summary of eight DFT calculations on the minimum and maximum bandgap configurations of $\text{Zn}_x\text{Cd}_{1-x}\text{Te}$. For each x , the bandgaps (BGs) and hole masses in both the [100] and [001] directions m_h^* are given. Electron effective masses in both directions are constant: $m_{e,100}^* = m_{e,001}^* = 0.1$. Effective masses are reported relative to the electron resting mass. HSE06 was used for the calculation of the bandgaps, and GGA was used for effective masses.

| x | Minimum gap | | | Maximum gap | | |
|------|-------------|---------------|---------------|-------------|---------------|---------------|
| | BG (eV) | $m_{h,100}^*$ | $m_{h,001}^*$ | BG (eV) | $m_{h,100}^*$ | $m_{h,001}^*$ |
| 0.00 | 1.36 | 0.6 | 0.6 | ... | ... | ... |
| 0.25 | 1.36 | 0.6 | 0.8 | 1.44 | 0.6 | 0.6 |
| 0.50 | 1.44 | 1.0 | 1.6 | 1.57 | 0.3 | 0.6 |
| 0.75 | 1.61 | 0.6 | 2.1 | 1.72 | 0.5 | 0.6 |
| 1.00 | 1.94 | 0.5 | 0.5 | ... | ... | ... |

in CdTe and ZnTe to 1.5 and 2.0 eV, respectively—identical to the EPM values. This constant shift would not, however, change the discrepancy between the EPM and DFT’s predictions of the difference in BG values between the minimum and maximum BG structures: GGA’s maximum variance is about 0.1 eV, although it still occurs at $x \approx 0.5$. The HSE06 pseudopotential does not change this result (see Table III), but it does cause the gaps of ZnTe and CdTe to match both experimental values and our EPM values. This discrepancy is due to the treatment of tellurium charge transfer described in Sec. II C, Eq. (10). If the best fit tellurium EPM potentials were more similar to one another, the EPM-predicted differences in gaps between the minimum and maximum BG structures would be more similar to the DFT results.

Both the EPM and DFT predict a nonlinear relationship between the BG and zinc concentration. This nonlinearity is well-known to occur in $\text{Zn}_x\text{Cd}_{1-x}\text{Te}$ and is described by the bowing parameter B in the equation $E_{g(\text{Zn,Cd})\text{Te}} = xE_{g,\text{ZnTe}} + (1-x)E_{g,\text{CdTe}} - x(1-x)B$.^{25–27} For the EPM, B is calculated to be 1.3, 1.0, and 0.6 eV for the minimum, average, and maximum BG structures, respectively. DFT GGA (HSE06) predicts B as 0.7 and 0.3 eV (0.9 and 0.3 eV) for the minimum and maximum BG structures. Reasons for differences between the EPM and DFT include the fact that the EPM potential was fit to experimental material data instead of atomic data and the fact that charge transfer in the EPM is simulated by the method described in Sec. II C. Zelaya-Angel *et al.*²⁵ have compiled a comprehensive table of experimental bowing parameters for $\text{Zn}_x\text{Cd}_{1-x}\text{Te}$. From it, the measured values of B range from 0.0 to 0.9 eV. Other theoretical calculations of B in $\text{Zn}_x\text{Cd}_{1-x}\text{Te}$ random alloys include predictions from empirical tight binding and DFT with various functionals, yielding values of B ranging from 0.2 to 1.6 eV.^{31–33,35,36} Overall, both our EPM and DFT predictions of B for the maximum BG structures fall within the experimental range of B as well as most theoretical predictions, despite the fact that our results are exclusively for layered $\text{Zn}_x\text{Cd}_{1-x}\text{Te}$ superlattices. The same is not true for the minimum BG structures, where our predicted B is generally higher than average. This is because the maximum BG structures are more similar to random alloys than the minimum BG structures are—see Table II.

Table II summarizes the results of DFT GGA calculations on the minimum and maximum BG cells found through the EPM search. It gives the layering orders of zinc and cadmium as well as lattice constants and formation energies for each structure. Figure 4 shows three example maximum BG structures, which correspond to the table entries for $x = 0.25, 0.50, 0.75$. The minimum BG

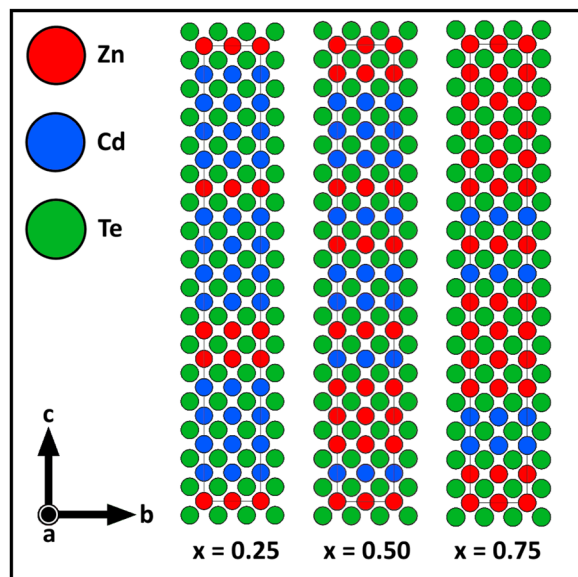


FIG. 4. Some predicted maximum-bandgap layering configurations of $\text{Zn}_x\text{Cd}_{1-x}\text{Te}$.

configurations are almost all bulk ZnTe and bulk CdTe, minimizing the number of ZnTe and CdTe interfaces as much as possible given stoichiometry and periodic boundary conditions. Technical exceptions are for $x = 0.1875, 0.3125, 0.3750$, and 0.8750 , of which each has the second smallest number of ZnTe/CdTe interfaces possible. The BG differences between these structures and the ones that minimize the number of interfaces are 1.4, 0.9, 0.5, and 7.8 meV for $x = 0.1875, 0.3125, 0.3750$, and 0.8750 , respectively. Given that all these differences are smaller than the tolerances that we set for the solutions to the FSM (10 meV), it seems reasonable to conclude that these are numerical errors, and the structures that truly minimize BG are those that minimize the number of ZnTe/CdTe interfaces. While one could predict the structures that minimized BG without the FSM, the structures that maximize BG are non-obvious. They do not maximize the number of ZnTe/CdTe interfaces, but instead have small clusters of ZnTe and CdTe somewhat-evenly distributed throughout the supercell.

The lattice constants in general decrease as x increases linearly, in agreement with available experiment^{26–28} and theory.^{31,33,35} In addition, the lattice constants of ZnTe (6.2 Å) and CdTe (6.6 Å) are about 2% larger than the experimental values, which is expected for DFT calculations. Comparing the minimum and maximum BG structures for a given x , the structures that minimize the gap tend to have larger lattice constants than those that maximize the gap. These differences in lattice constant are not constant, ranging from 0.02 to 0.05 Å, with the larger differences tending to be closer to $x = 0.5$. While zinc concentration is the major contributor to the lattice constant, it is clear that the layer orderings have some effect as well.

The formation energies of $\text{Zn}_x\text{Cd}_{1-x}\text{Te}$ superlattices are all negative, equal to about -1 eV per formula unit (f.u.), indicating that these structures should be able to be synthesized. The energies tend to grow larger as x approaches 0.5: about a 30 and 15 meV/f.u.

increase from ZnTe and CdTe, respectively. At any given x , the maximum BG configuration is lower in energy than the minimum BG configuration by 1 to 2 meV/f.u. There is no trend in these energy differences.

C. Crystal orbital Hamilton populations

Results of the COHP analysis on the minimum and maximum BG models, computed with DFT-HSE06, for a few zinc concentrations are shown in Fig. 5. We plot the first-nearest-neighbor contributions to the negative partial COHP ($-p\text{COHP}$) (Zn–Te and Cd–Te pairs) so that bonding contributions are shown as positive in Fig. 5. Only compounds including both zinc and cadmium are shown here; see the supplementary material (Fig. S2) for the $-p\text{COHP}$ of ZnTe and CdTe. The insets of Fig. 5 show the energy regions near the VBMs and CBMs.

Overall, states near the Fermi level have little/no antibonding contributions, being outweighed by the large bonding contributions lower in energy, confirming that Zn–Te and Cd–Te bonds are both stable. As a function of x , the amount of Zn–Te population increases as the concentration of Zn increases. In addition, as [Zn] climbs, the integral of the COHP up to the VBM becomes more negative: from an average of -1.37 at $x = 0.25$ to -1.41 at $x = 0.50$ and finally -1.45 at $x = 0.75$. This signifies that $\text{Zn}_x\text{Cd}_{1-x}\text{Te}$ is predicted to become slightly more stable with increasing [Zn].

Concerning similarities and differences between minimum and maximum BG structures, the valence bands near the Fermi level are almost indistinguishable from one another. Valence bands lower in energy show differences, but no visible systematic trends. The superlattices that maximize the gap do, however, have slightly more negative bonding population values, quantified by the integrals of the COHP up to the VBMs: for $x = 0.25$, these values are -1.35 and -1.38 for the minimum and maximum BG structures, respectively.

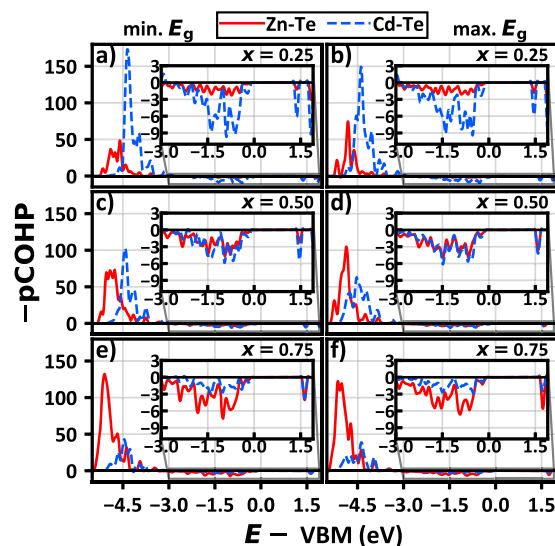


FIG. 5. Negative $p\text{COHP}$ plots for minimum [(a), (c), and (e)] and maximum [(b), (d), and (f)] bandgap $\text{Zn}_x\text{Cd}_{1-x}\text{Te}$ configurations, split into contributions from Zn–Te (red solid lines) and Cd–Te (blue dashed lines), calculated with HSE06. The $-p\text{COHP}$ is plotted so that bonding contributions are positive on the graphs.

Similarly, for $x = 0.50$ and $x = 0.75$, the integrals of the COHPs are -1.39 (-1.42) and -1.44 (-1.45) for the minimum BG lattice (maximum BG lattice). This fact is in agreement with the formation energies of Table II, where structures that maximize the gap are slightly lower in energy than those that minimize the gap.

In all cases, the contributions to the COHP from Zn–Te pairs are slightly higher ($+0.2\%$) for the maximum BG structures than they are for the minimum gap structures. Conversely, the Cd–Te pair contributions to the COHP are slightly lower (-0.2%) for the maximum bandgap structures compared to the structures that minimize the gap. Most tellurium atoms in the minimum BG configurations are completely surrounded by either zinc or cadmium, while tellurium in the maximum gap structures may be coordinated by all zinc, all cadmium, or a mix of the two. This implies that Zn–Te bonds in the mixed Zn/Cd regions of $\text{Zn}_x\text{Cd}_{1-x}\text{Te}$ superlattices are stronger than Zn–Te bonds in the phase-separated ZnTe regions of the superlattice. The opposite is true for Cd–Te bonds. Possibly, the increase in bonding strength of zinc bonds outweighs the decrease in bonding strength of cadmium bonds, which explains why the structures that maximize the bandgap have lower formation energies. As will be explained in Sec. III D, this effect can be explained by the effect of local atomic environment on the density of states of tellurium atoms.

There are also differences in the conduction band populations, most noticeable for $x = 0.50, 0.75$. These differences seem to arise more from the density of states itself, discussed in Sec. III D, than the overlap between bonding energies and the density of states.

D. Densities of states

Figure 6 shows the orbital-decomposed DOS of the minimum and maximum BG configurations for some zinc concentrations as computed by DFT–HSE06. The s , p , and d states of zinc, cadmium, and tellurium are all indicated since each has a significant contribution, other than the d states of tellurium. Note that the x -axis is broken at the VBM in order to more clearly show the conduction band states. Only compounds including both zinc and cadmium are shown in Fig. 6; see Fig. S3 of the supplementary material for the DOS of ZnTe and CdTe.

In general, the valence bands are dominated by the p states of tellurium. The p and d states of zinc and/or cadmium are the only other major contributors to the valence band DOS, depending on stoichiometry. The conduction band DOS is comprised of the s states of zinc and/or cadmium as well as the s states of tellurium. The relative contributions to the DOS are in agreement with previous theoretical work on $\text{Zn}_x\text{Cd}_{1-x}\text{Te}$.³¹ Compared to the conduction bands, the valence bands have a sharper onset at the VBM, indicating that they are flatter than the conduction bands. This is in agreement with the effective masses listed in Table III, where the hole masses are 3 to 10 times heavier than the electron masses.

We have also investigated how the local environment of tellurium affects its contributions to the DOS in Fig. 7 (again, computed within DFT–HSE06). Figures 7(a) and 7(b) show the valence and conduction band edges, respectively. Only the s and p states are shown, as the d states of tellurium are noncontributing within the energy range of interest. The differing colors represent tellurium in different local environments: red and blue for tellurium surrounded

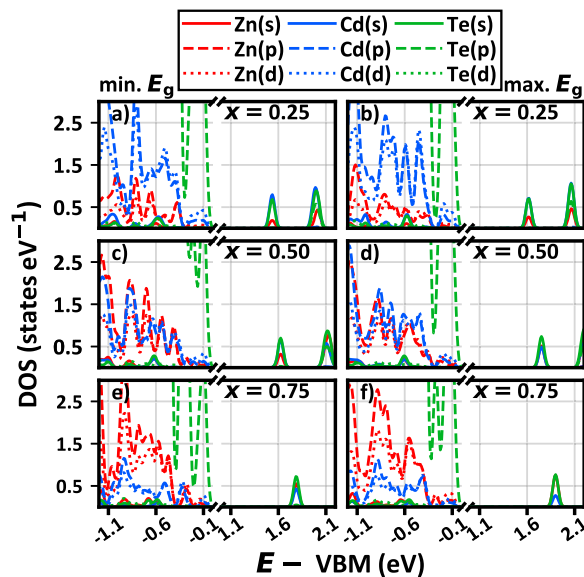


FIG. 6. DOS plots for minimum [(a), (c), and (e)] and maximum [(b), (d), and (f)] bandgap $\text{Zn}_x\text{Cd}_{1-x}\text{Te}$ configurations calculated with HSE06. The DOS is split into contributions from zinc (red), cadmium (blue), and tellurium (green) atoms as well as their s (solid), p (dashed), and d (dotted) states. Note that the energy axes are broken after the valence band maxima to more clearly show band edge states.

completely by zinc and cadmium, respectively. Green represents tellurium surrounded by half zinc and half cadmium. Here, tellurium is treated as three separate species in the same way as was done for the EPM, and the DOS is normalized by the count of each “unique” species. Also note the differences in scale: the valence band DOS is around six times larger than the conduction band DOS.

The differences in the DOS depending on local environment exemplify our reasoning for using three different tellurium potentials: the s and p states of tellurium are sensitive to what atoms it is bonded to. Regarding valence bands in Fig. 7(a), as the number of cadmium neighbors increases, the p states of tellurium contribute more to the DOS. From Fig. 7(b), it can be seen that the conduction band s states of tellurium are also directly correlated with the increase in cadmium nearest neighbors. Interestingly, in the conduction band, the p state DOS of tellurium is the same regardless of whether tellurium is surrounded completely by zinc or cadmium. If tellurium has two bonds with zinc and two bonds with cadmium, however, its p states are more numerous. This effect is too small to be resolvable in Fig. 6.

The effect of atomic ordering on the valence band edges of the DOS can be explained through Fig. 7. Since tellurium p states make up most of the valence band edge, it is easiest to see the following effects through the total DOS, shown in Fig. S4. In the following, we will denote a tellurium surrounded by N_{Zn} zinc atoms and N_{Cd} cadmium atoms as $\text{Te}[N_{\text{Zn}}\text{Zn}, N_{\text{Cd}}\text{Cd}]$.

At any given value of x , the configuration that minimizes the gap has a smaller number of $\text{Te}[2\text{Zn}, 2\text{Cd}]$ than the max BG structure does. For low zinc concentrations ($x \leq 0.25$), the number of $\text{Te}[4\text{Zn}, 0\text{Cd}]$ is negligible for both the structures that minimize and maximize the bandgap. So, the transition from the structure with

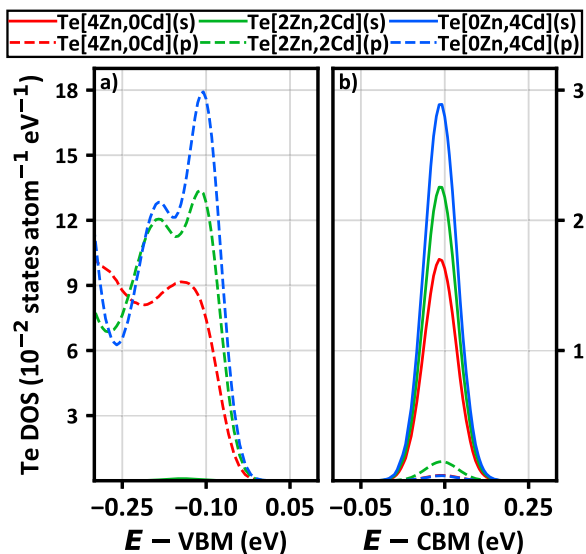


FIG. 7. Dependence of local environment on the DOS of tellurium atoms in $\text{Zn}_x\text{Cd}_{1-x}\text{Te}$ calculated with HSE06. The *s* (solid lines) and *p* (dashed lines) states of tellurium in all three possible local environments (four, two, and zero zinc bonds as red, green, and blue lines, respectively) are averaged over the minimum and maximum bandgap configurations for $x = 0.25, 0.50, 0.75$. Only states near (a) the valence band edge and (b) the conduction band edge are shown.

the minimum gap to the structure with the maximum gap only exchanges Te[0Zn, 4Cd] for Te[2Zn, 2Cd]. The former contribute more to the valence band edge DOS than the latter. Therefore, the valence band edge is larger for the minimum gap configurations compared to the maximum gap configurations. By a similar argument, high zinc concentrations ($x \geq 0.75$) exhibit a valence band DOS, which is larger for configurations that maximize the gap compared to the minimal BG structures since Te[2Zn, 2Cd] has a larger DOS profile than Te[4Zn, 0Cd]. Finally, for intermediate zinc concentrations ($0.25 \leq x \leq 0.75$), the valence band edge DOS is roughly the same between the minimum and maximum BG structures. This is because the DOS contribution of Te[2Zn, 2Cd] is about equal to the average of Te[0Zn, 4Cd] and Te[4Zn, 0Cd], and about an equal number of Te[0Zn, 4Cd] and Te[4Zn, 0Cd] are exchanged for Te[2Zn, 2Cd] when transitioning from the minimum to the maximum gap configurations.

The previous discussion about the valence band edge also applies to tellurium's *s*-state contribution to the conduction band edge, although this is complicated by the fact that both zinc and cadmium's *s* states participate non-negligibly to the conduction band DOS as well. Zinc contributes more states to the band edge DOS in the maximum BG structures than in those that minimize the gap. The cadmium atoms contribute less states in the maximum BG structures than in the minimum BG structures.

E. Effective masses

In Table III are the values of the effective electron and hole masses calculated parallel ([100] direction, *a* or *b* in Fig. 4) and perpendicular ([001] direction, *c* in Fig. 4) to the stacked layers in our

$\text{Zn}_x\text{Cd}_{1-x}\text{Te}$ superlattices. These values are computed with DFT-GGA using the standard quadratic approximation to the energy dispersion relationships. All effective mass values in Table III and in this section are reported as fractions of the electron resting mass.

The effective masses of electrons, m_e^* , are 0.1 for both ZnTe and CdTe. Holes, m_h^* , are calculated to be heavier, 0.5 for ZnTe and 0.6 for CdTe. Our results for m_e^* are in excellent agreement with experimental results for both ZnTe, equal to 0.1 and 0.2,^{82,83} and CdTe, equal to 0.1.^{84,85} Theoretical calculations of m_e^* in ZnTe include 0.1 and 1.3: the former along [100] and the latter an average over high-symmetry paths.^{31,86} The comparison of m_h^* is complicated by the degeneracy of $\text{Zn}_x\text{Cd}_{1-x}\text{Te}$ at the Γ point. m_h^* measurements give 0.2 for ZnTe and 0.4–0.6 for CdTe.^{14,84,85} Our calculations of m_h^* in ZnTe differ from experimental results by 0.3, while our value for CdTe is within the range of experimental measurements. Furthermore, our calculations agree with the trend that m_h^* is heavier in CdTe than in ZnTe. Paiva *et al.* calculated light and heavy holes in ZnTe to be 0.1 and 0.4, respectively, and Dumre *et al.* found an average of 1.2.^{31,86} These same values for CdTe are 0.1, 0.5, and 1.3. Our calculated m_h^* are very similar to the heavy hole calculations of Pavia *et al.*, but differ significantly from those of Dumre *et al.*

As both a function of zinc concentration and differences in atomic configurations between the minimum and maximum BG structures, our calculated m_e^* is constant, equal to 0.1. This indicates that the shape of the conduction bands is insensitive to x and possibly to changes in atomic structure as well. The behavior of m_h^* is more complicated, not seeming to follow any consistent trend. For example, m_h^* in the [100] direction for the minimum BG configurations is heaviest at $x = 0.5$, but the same mass vs x relationship for the maximum BG configurations is at its minimum for $x = 0.5$. In addition, m_h^* in the [001] direction has a high variance with x for the structures that minimize BG, but no variance for the structures that maximize BG. At any given zinc concentration, the relationship between minimum BG structures and maximum BG structures is unpredictable—a result of the seemingly unpredictable layering configurations of the maximum BG structures.

F. Absorption and reflectivity spectra

Figure 8 shows both the absorption and reflectivity spectra of minimum and maximum BG $\text{Zn}_x\text{Cd}_{1-x}\text{Te}$ superlattices over the energy range of interest for PV applications, computed with DFT-HSE06. The spectra are both calculated from the average of the diagonals of the dielectric response matrix. In addition, the AM 1.5G solar spectra are shown in the backgrounds.^{87,88} Only compounds including both zinc and cadmium are shown in Fig. 8; see Fig. S5 of the supplementary material for the absorption and reflectivity spectra of ZnTe and CdTe.

In general, the absorption coefficient α is found to be between 10^4 and 10^5 cm^{-1} until $\hbar\omega \approx 3.5$ eV, at which point it rapidly increases. The reflectivities R range from 20% to 35% within the energy range of interest. These values are in good agreement with experimental measurements of Sato and Adachi,⁸⁹ who obtained α for ZnTe to be 1.2×10^4 and 1.2×10^5 cm^{-1} at $\hbar\omega = 2.3$ and 3.5 eV, respectively, as well as $R = 23\%$ and 40% at $\hbar\omega = 1.5$ and 3.5 eV, respectively. Rangel-Cárdenas and Sobral⁹⁰ measured α in CdTe as 2.3×10^4 cm^{-1} and 2.9×10^4 cm^{-1} and R as 23% and 30%. Both of these values are for $\hbar\omega = 1.6$ and 3.1 eV and compare well with

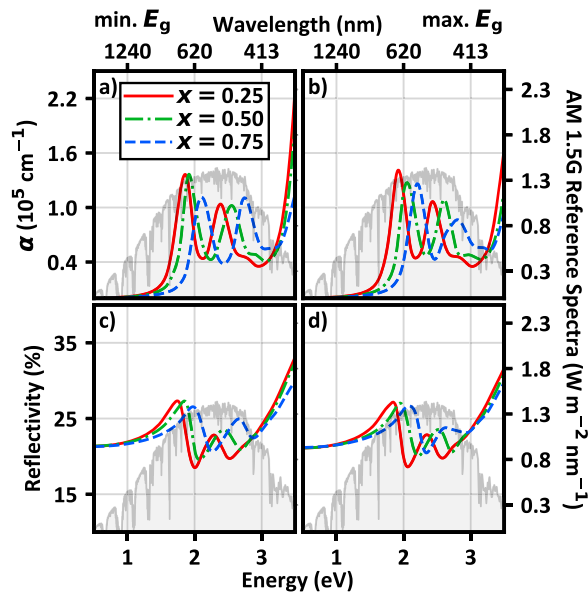


FIG. 8. (a) and (b) Absorption coefficient α and (c) and (d) reflectivity spectra for minimum [(a) and (c)] and maximum [(b) and (d)] bandgap $\text{Zn}_x\text{Cd}_{1-x}\text{Te}$ configurations calculated with HSE06. The response functions for $x = 0.25, 0.50, 0.75$ (red solid, green dotted-dashed, and blue dashed lines, respectively) correspond to the left-hand axes. They overlay the AM 1.5G solar spectra, shown in gray, of which the scales are on the right-hand axes.

our calculations for both alloys and their end members. Dumre *et al.*³¹ provide both α and R as a function of x in $\text{Zn}_x\text{Cd}_{1-x}\text{Te}$ random alloys, calculated with DFT-HSE06. Their calculated values also match our results.

Changes in the response functions with x are regular, with the major features of α and R shifting to higher energies as zinc concentration increases due to the increasing bandgap. In addition, as x increases, the minima of α and R increase, while their maxima tend to decrease. Dumre *et al.*³¹ report less regular changes in the optical characteristics as a function of x . This discrepancy can be explained by the significant differences in simulation cells between the present study (layered superlattices) and theirs (random alloys).

Both α and R are, overall, very similar when comparing the minimum and maximum BG structures. They exhibit blueshifting of major features due to changes in bandgap, though to a lesser extent than the shifting discussed in the previous paragraph. There are otherwise many small differences (unlikely to be perceivable in an experimental setting), but no noticeable trends. For example, at $x = 0.25, 0.50$, the first peak of the minimum BG α spectra is shorter and wider than the corresponding peak for the maximum BG structure's α . The opposite is true of the second peak of the $x = 0.75$ structures. Comparison between the R spectra of different atomic configurations is less obvious than the α response. The most notable feature would be the difference in shape and magnitude of R for the $x = 0.75$ set of configurations near $\hbar\omega = 2.6$ eV.

IV. CONCLUSION

In this work, we employed a valence force field model paired with the EPM + FSM to efficiently explore the large search space

of $\text{Zn}_x\text{Cd}_{1-x}\text{Te}$ 32-layer superlattices and determine the structures that minimize and maximize BG at each possible value of x . In doing so, we identified convergence issues present when pairing the LOBPCG method with the usual FSM preconditioner and small subspace size. We then demonstrated that using an alternative preconditioner solves the convergence issues, which should allow for more widespread application of the FSM.

We also examined a few $\text{Zn}_x\text{Cd}_{1-x}\text{Te}$ structures and calculated their physical properties with hybrid DFT. Formation energy estimations of each structure, as well as analysis of the COHP, indicated that each structure was stable. We found the bandgap bowing for high BG superlattices ($B = 0.6$ eV) to be similar to experimental and theoretical results, while the bowing for small BG structures ($B = 1.3$ eV) was larger.^{25–27,31–33,35,36} At any given zinc concentration, the atomic structure of $\text{Zn}_x\text{Cd}_{1-x}\text{Te}$ superlattices was found to significantly affect the effective masses. The optical response functions, however, were found to depend very little on specifics of atomic structure, instead varying mostly with x .

The ability to tune the bandgap by up to 0.2 eV, independent of zinc concentration, could be used to counteract the bandgap-lowering reaction of zinc with CdCl_2 in $\text{Zn}_x\text{Cd}_{1-x}\text{Te}$ devices.²⁴ The ordering of the atomic layers has little effect on the lattice constants. This, paired with the variance of the bandgap, would make lattice matching simpler. Furthermore, physical quantities other than BG may be well-suited for the method. The dependence of the effective masses on atomic structure, as well as their importance for charge carrier transport, indicates that an EPM-based exploration or optimization of the effective mass would be a useful tool for designing high-quality superlattices. It may also be possible to use the EPM + FSM to optimize spectral properties such as the DOS or optical response functions within a certain energy range. In particular, absorption and reflective characteristics of PV devices are of importance. One may design a superlattice that maximizes the absorption coefficient, allowing for a thinner absorber layer. The reflectivity of $\text{Zn}_x\text{Cd}_{1-x}\text{Te}$ increases steadily as photon energies approach the UV range. Certain orderings of atomic layers may be able to minimize this effect.

The results of this study attest to the usefulness of the EPM + FSM in optimization problems that would otherwise be intractable with present-day computational resources. Even more difficult problems may be solved with global optimization techniques,^{12,15} which is a logical next step for future work.

SUPPLEMENTARY MATERIAL

The [supplementary material](#) contains explicit modifications made to the preconditioner of Teter *et al.*⁷⁷ Keating force field parameters as well as the band structures, crystal orbital Hamilton populations, densities of states, and optical response functions for ZnTe and CdTe are also provided.

ACKNOWLEDGMENTS

This material is based on research sponsored by the Air Force Research Laboratory under Agreement No. FA9453-21-C-0056. The U.S. Government is authorized to reproduce and distribute reprints

for governmental purposes notwithstanding any copyright notation thereon. The views expressed are those of the authors and do not reflect the official guidance or position of the United States Government, the Department of Defense or of the United States Air Force. The appearance of external hyperlinks does not constitute endorsement by the United States Department of Defense (DoD) of the linked websites, or the information, products, or services contained therein. The DoD does not exercise any editorial, security, or other control over the information you may find at these locations. Approved for public release; distribution is unlimited. Public Affairs release approval Grant No. AFRL-2024-2826.

The calculations for this research were performed on the Ohio Supercomputer Center's Owens cluster⁹¹ and the University of Toledo's computing clusters.

AUTHOR DECLARATIONS

Conflict of Interest

The authors have no conflicts to disclose.

Author Contributions

V. Barone: Conceptualization (equal); Investigation (equal); Methodology (equal); Software (equal); Validation (equal); Visualization (equal); Writing – original draft (equal); Writing – review & editing (equal). **R. J. Ellingson:** Conceptualization (equal); Funding acquisition (equal); Project administration (equal). **S. V. Khare:** Conceptualization (equal); Funding acquisition (equal); Project administration (equal); Resources (equal); Supervision (equal); Writing – original draft (equal); Writing – review & editing (equal).

DATA AVAILABILITY

The data that support the findings of this study are available from the corresponding author upon reasonable request.

APPENDIX A: KEATING FORCE FIELD EQUATIONS

The Keating model⁴⁷ of strain in a solid assigns an energy V to each atom i located at position \mathbf{x}_i . $V(\mathbf{x}_i)$ includes two-term bond length contributions and three-term bond angle contributions as follows:

$$V(\mathbf{x}_i) = \frac{1}{N_{\text{pairs}}} \sum_j \left[\frac{\alpha_{ij}}{r_{0,ij}^2} (\mathbf{x}_{ij} \cdot \mathbf{x}_{ij} - r_{0,ij}^2)^2 + \frac{1}{N_{\text{triplets}}} \times \sum_{k \neq j} \frac{\beta_{jik}}{r_{0,ij} r_{0,ik}} (\mathbf{x}_{ij} \cdot \mathbf{x}_{ij} - r_{0,ij} r_{0,ik} \cos(\theta_{0,jik}))^2 \right], \quad (\text{A1})$$

where $\mathbf{x}_{ij} \equiv \mathbf{x}_j - \mathbf{x}_i$, $r_{0,ij}$ is the ideal bond distance for atoms i and j , and $\theta_{0,jik}$ is the ideal bond angle between bond $i-j$ and bond $i-k$. The force constants α_{ij} and β_{jik} are to be fit to match some reference data. The sum j runs over every first nearest-neighbor of atom i (pairs), and the sum k runs over each first nearest-neighbor of atom i excluding j (triplets).

By applying $\mathbf{F} = -\nabla V$, the force on atom i can be obtained as

$$\mathbf{F}(\mathbf{x}_i) = \sum_j^{N_{\text{pairs}}} \left[\mathbf{x}_{ij} C_{ij} + \sum_{k \neq j}^{N_{\text{triplets}}} (\mathbf{x}_{ij} + \mathbf{x}_{ik}) C_{ijk} \right],$$

$$C_{ij} \equiv \frac{4}{N_{\text{pairs}}} \alpha_{ij} \left(\frac{|\mathbf{x}_{ij}|^2}{r_{0,ij}^2} - 1 \right), \quad (\text{A2})$$

$$C_{ijk} \equiv \frac{2}{N_{\text{pairs}} N_{\text{triplets}}} \sqrt{\beta_{ij} \beta_{ik}} \left(\frac{\mathbf{x}_{ij} \cdot \mathbf{x}_{ik}}{r_{0,ij} r_{0,ik}} - \cos(\theta_{0,jik}) \right).$$

We have also made the simplification that $\beta_{jik} \approx \sqrt{\beta_{ij} \beta_{ik}}$ to reduce the number of force constants to fit. This simplification is well founded. It is, for example, the default mixing rule used in the large-scale atomic/molecular massively parallel simulator.⁹²

APPENDIX B: EMPIRICAL PSEUDOPOTENTIAL EQUATIONS

The pseudopotential form chosen used in this study is a combination of an empty core model similar to that of Ashcroft⁹³ and an empirical form derived from the one used by Kimball *et al.*⁹⁴

Ashcroft's model, in atomic units, is $v(q) = -3/2E_F \lambda^2 \cos(py)/(y^2 + \lambda^2 g(y))$. The full description of each parameter is given by Ashcroft, Cohen, and Heine.^{68,93} The version that we use replaces the screening term in the denominator by a similar form, which allows for fine adjustments of v , especially near q_0 . In standard units, it reads

$$v_1(q) = v_0 \frac{\cos\left(\frac{\pi q}{2 q_0}\right)}{1 + (sq)^2}, \quad (\text{B1})$$

where $v_0 \equiv v_1(q = q_0)$, q_0 is the q corresponding to the first zero of v , and s is an adjustable parameter controlling the screening. We use this form since it is similar to the empty core model for small q , but includes three adjustable parameters instead of one. v_0 should be chosen (but may be adjusted slightly) as $-3/2$ the free electron Fermi energy, q_0 can be derived by existing data, such as the tabulated form factors from Cohen and Heine,⁶⁸ and s is expected to be less than 1 Å.

Kimball *et al.*⁹⁴ used the form $v(q) = A(q - q_0) \exp[-B(q - q_0)]$. A and B are adjustable parameters, and q_0 is the q corresponding to the first zero of v . The form that we use, obtained by replacing A and B (as well as adding a new parameter n), is similar,

$$v_2(q) = v_m \left(\frac{q - q_0}{q_m - q_0} \right)^n \exp \left[1 - \left(\frac{q - q_0}{q_m - q_0} \right)^n \right]. \quad (\text{B2})$$

Here, v_m is the first maxima of v past q_0 and q_m is the value of q corresponding to v_m . n is an adjustable parameter that affects the width of v . We prefer this form since the values q_0 , q_m , and v_m are easily chosen from existing data, such as the tabulated form factors from Cohen and Heine.⁶⁸ In addition, n is expected to be close to 1.0, but may be adjusted.

The Ashcroft model alone does not provide the necessary accuracy for describing band structures, but the Kimball form is not

appropriate for the low values of q sampled by large lattices. In addition, the introduction of n into v_2 , while useful for adjusting the potential, can result in numerical issues for $q < q_0$. Thus, the actual potential that we use is a smoothed piecewise-defined function,

$$v(q) = \frac{1}{2l} \int_{q-l}^{q+l} v_{12}(x') \Theta(x') dx', \quad (B3)$$
$$v_{12}(q) = \begin{cases} v_1, & 0 < q < q_0, \\ v_2, & q_0 < q. \end{cases}$$

The window length l must be chosen large enough that it provides adequate smoothing of the discontinuity at q_0 but small enough that it does not affect the form of v_{12} too heavily. We have also introduced Θ , a cutoff function, used to ensure that $v \rightarrow 0$ at $q = q_c$, the q corresponding to the cutoff energy. A general form of the cutoff function is

$$\Theta(q) = \frac{1}{2} \left\{ 1 + \tanh \left[\frac{r}{1-f} \left(f + \frac{q_m - q}{q_c - q_m} \right) \right] \right\}, \quad (B4)$$

where r (unitless, $0 < r < \infty$) controls how rapidly Θ approaches zero and f (unitless, $0 \leq f < 1$) is the fractional distance between q_m and q_c of the position at which $\Theta = 1/2$.

REFERENCES

- J. F. Geisz, M. A. Steiner, I. Garcia, S. R. Kurtz, and D. J. Friedman, "Enhanced external radiative efficiency for 20.8% efficient single-junction GaInP solar cells," *Appl. Phys. Lett.* **103**, 041118 (2013).
- E. E. Perl, J. Simon, J. F. Geisz, W. Olavarria, M. Young, A. Duda, D. J. Friedman, and M. A. Steiner, "Development of high-bandgap AlGaInP solar cells grown by organometallic vapor-phase epitaxy," *IEEE J. Photovoltaics* **6**, 770–776 (2016).
- A. Qasem, B. Alshahrani, H. A. Yakout, H.-A. S. Abbas, and E. R. Shaaban, "Tuning structural, optical, electrical and photovoltaic characteristics of n-type CdS_{1-x}Sb_x layers for optimizing the performance of n-(CdS:Sb)/p-Si solar cells," *Appl. Phys. A* **127**, 849 (2021).
- N. Romeo, A. Bosio, V. Canevari, and A. Podestà, "Recent progress on CdTe/CdS thin film solar cells," *Sol. Energy* **77**, 795–801 (2004).
- H. Shibata, J. Nishinaga, Y. Kamikawa, H. Tampo, T. Nagai, T. Koida, S. Ishizuka, T. Mochizuki, and M. Yamaguchi, "Experimental confirmation of the optoelectronic reciprocity theorem in high-efficiency CuIn_{1-x}Ga_xSe₂ solar cells," *Phys. Rev. Appl.* **19**, 054072 (2023).
- B. Wang, M. Zhang, V. Adhikari, P. Fang, S. V. Khare, and D. Gall, "Bandgap and strain engineering in epitaxial rocksalt structure (Ti_{0.5}Mg_{0.5})_{1-x}Al_xN(001) semiconductors," *J. Mater. Chem. C* **8**, 12677–12688 (2020).
- A. Cho and J. Arthur, "Molecular beam epitaxy," *Prog. Solid State Chem.* **10**, 157–191 (1975).
- J. E. Davey and T. Pankey, "Epitaxial GaAs films deposited by vacuum evaporation," *J. Appl. Phys.* **39**, 1941–1948 (1968).
- R. E. I. Schropp, B. Stannowski, and A. M. Brockhoff, "Hot wire CVD of heterogeneous and polycrystalline silicon semiconducting thin films for application in thin film transistors and solar cells," *Mater. Phys. Mech.* **1**, 73–82 (2000).
- I. A. Shareef, G. W. Rubloff, M. Anderle, W. N. Gill, J. Cotte, and D. H. Kim, "Subatmospheric chemical vapor deposition ozone/TEOS process for SiO₂ trench filling," *J. Vac. Sci. Technol., B: Microelectron. Nanometer Struct.–Process., Meas., Phenom.* **13**, 1888–1892 (1995).
- K. Y. S. Chang and O. A. Von Lilienfeld, "Al_xGa_{1-x}As crystals with direct 2 eV band gaps from computational alchemy," *Phys. Rev. Mater.* **2**, 073802 (2018).
- A. Franceschetti and A. Zunger, "The inverse band-structure problem of finding an atomic configuration with given electronic properties," *Nature* **402**, 60–63 (1999).
- J. Íñiguez and L. Bellaiche, "Ab initio design of perovskite alloys with predetermined properties: The case of Pb(SCo_{0.5}Nb_{0.5})O₃," *Phys. Rev. Lett.* **87**, 095503 (2001).
- G. H. Jóhannesson, T. Bligaard, A. V. Ruban, H. L. Skriver, K. W. Jacobsen, and J. K. Nørskov, "Combined electronic structure and evolutionary search approach to materials design," *Phys. Rev. Lett.* **88**, 255506 (2002).
- K. Kim, P. A. Graf, and W. B. Jones, "A genetic algorithm based inverse band structure method for semiconductor alloys," *J. Comput. Phys.* **208**, 735–760 (2005).
- P. Piquini, P. A. Graf, and A. Zunger, "Band-gap design of quaternary (In, Ga)(As, Sb) semiconductors via the inverse-band-structure approach," *Phys. Rev. Lett.* **100**, 186403 (2008).
- P. Piquini and A. Zunger, "Using superlattice ordering to reduce the band gap of random (In, Ga)As/InP alloys to a target value via the inverse band structure approach," *Phys. Rev. B* **78**, 161302 (2008).
- K. Prasai, P. Biswas, and D. A. Drabold, "Sculpting the band gap: A computational approach," *Sci. Rep.* **5**, 15522 (2015).
- P. Seller, S. Bell, R. J. Cernik, C. Christodoulou, C. K. Egan, J. A. Gaskin, S. Jacques, S. Pani, B. D. Ramsey, C. Reid, P. J. Sellin, J. W. Scuffham, R. D. Speller, M. D. Wilson, and M. C. Veale, "Pixellated Cd(Zn)Te high-energy X-ray instrument," *J. Instrum.* **6**, C12009 (2011).
- S. Del Sordo, L. Abbene, E. Caroli, A. M. Mancini, A. Zappettini, and P. Ubertini, "Progress in the development of CdTe and CdZnTe semiconductor radiation detectors for astrophysical and medical applications," *Sensors* **9**, 3491–3526 (2009).
- M. D. Wilson, R. Cernik, H. Chen, C. Hansson, K. Iniewski, L. L. Jones, P. Seller, and M. C. Veale, "Small pixel CZT detector for hard X-ray spectroscopy," *Nucl. Instrum. Methods Phys. Res., Sect. A* **652**, 158–161 (2011).
- S. Rühle, "Tabulated values of the Shockley–Queisser limit for single junction solar cells," *Sol. Energy* **130**, 139–147 (2016).
- W. Shockley and H. J. Queisser, "Detailed balance limit of efficiency of p - n junction solar cells," *J. Appl. Phys.* **32**, 510–519 (1961).
- F. K. Alfadhili, G. K. Liyanage, A. B. Phillips, and M. J. Heben, "Development of CdCl₂ activation to minimize Zn loss from sputtered Cd_{1-x}Zn_xTe thin films for use in tandem solar cells," *MRS Adv.* **3**, 3129–3134 (2018).
- O. Zelaya-Angel, J. G. Mendoza-Alvarez, M. Becerril, H. Navarro-Contreras, and L. Tirado-Meía, "On the bowing parameter in Cd_{1-x}Zn_xTe," *J. Appl. Phys.* **95**, 6284–6288 (2004).
- A. Aydinli, A. Compaan, G. Contreras-Puente, and A. Mason, "Polycrystalline Cd_{1-x}Zn_xTe thin films on glass by pulsed laser deposition," *Solid State Commun.* **80**, 465–468 (1991).
- A. Ebina, K. Saito, and T. Takahashi, "Crystal growth of Zn_xCd_{1-x}Te solid solutions and their optical properties at the photon energies of the lowest band-gap region," *J. Appl. Phys.* **44**, 3659–3662 (1973).
- K. P. Rao, O. M. Hussain, B. S. Naidu, and P. J. Reddy, "Electrical properties of two-source evaporated polycrystalline films," *Semicond. Sci. Technol.* **12**, 564–569 (1997).
- R. Triboulet, G. Neu, and B. Fotouhi, "Growth and characterization of the complete Cd_{1-x}Zn_xTe alloy series," *J. Cryst. Growth* **65**, 262–269 (1983).
- Y. Znamenshchikov, V. Kosyak, O. Kononov, I. Shpetnyi, V. Grebinaha, P. Fochuk, and A. Opanasyuk, "Electrical, structural and optical properties of Cd_{1-x}Zn_xTe thick polycrystalline films," *Vacuum* **149**, 270–278 (2018).
- B. Dumre, R. Ellingson, and S. Khare, "Effects of short-range order on phase equilibria and opto-electronic properties of ternary alloy Zn_xCd_{1-x}Te," *Sol. Energy Mater. Sol. Cells* **248**, 111971 (2022).
- I. Khan, H. R. Aliabad, W. Ahmad, Z. Ali, and I. Ahmad, "First principle optoelectronic studies of visible light sensitive CZT," *Superlattices Microstruct.* **63**, 91–99 (2013).
- A. Merad, M. Kanoun, G. Merad, and J. Cibert, "Theoretical analysis of the bowing factors in electronic and optical properties in Cd_{1-x}Zn_xTe alloys," *Rev. Energ. Ren. ICPWE*, 107–111 (2003).
- K. Mimouni, N. Mokdad, K. Beladjal, A. Kadri, and K. Zitouni, "Energy bandgap of Cd_{1-x}Zn_xTe, Cd_{1-x}Zn_xSe and Cd_{1-x}Zn_xS semiconductors: A first-principles analysis based on Tran–Blaha–Modified Becke–Johnson exchange potential," *J. Electron. Mater.* **52**, 4191–4201 (2023).

- ³⁵H. Rozale, A. Lazreg, A. Chahed, and P. Ruterana, "Structural, electronic and optical properties of the wide-gap ternary alloys," *Superlattices Microstruct.* **46**, 554–562 (2009).
- ³⁶J.-H. Yang, S. Chen, W.-J. Yin, X. G. Gong, A. Walsh, and S.-H. Wei, "Electronic structure and phase stability of MgTe, ZnTe, CdTe, and their alloys in the B3, B4, and B8 structures," *Phys. Rev. B* **79**, 245202 (2009).
- ³⁷D. K. Ward, X. W. Zhou, B. M. Wong, F. P. Doty, and J. A. Zimmerman, "Analytical bond-order potential for the Cd–Zn–Te ternary system," *Phys. Rev. B* **86**, 245203 (2012).
- ³⁸D. K. Ward, X. Zhou, B. M. Wong, and F. P. Doty, "A refined parameterization of the analytical Cd–Zn–Te bond-order potential," *J. Mol. Model.* **19**, 5469–5477 (2013).
- ³⁹F. Aryasetiawan and O. Gunnarsson, "The GW method," *Rep. Prog. Phys.* **61**, 237–312 (1998).
- ⁴⁰W. M. C. Foulkes, L. Mitás, R. J. Needs, and G. Rajagopal, "Quantum Monte Carlo simulations of solids," *Rev. Mod. Phys.* **73**, 33–83 (2001).
- ⁴¹T. Gruber, K. Liao, T. Tsatsoulis, F. Hummel, and A. Grüneis, "Applying the coupled-cluster ansatz to solids and surfaces in the thermodynamic limit," *Phys. Rev. X* **8**, 021043 (2018).
- ⁴²L. Hedin, "New method for calculating the one-particle Green's function with application to the electron-gas problem," *Phys. Rev.* **139**, A796–A823 (1965).
- ⁴³J. Kolorenč and L. Mitás, "Applications of quantum Monte Carlo methods in condensed systems," *Rep. Prog. Phys.* **74**, 026502 (2011).
- ⁴⁴J. P. Perdew, "Density functional theory and the band gap problem," *Int. J. Quantum Chem.* **28**, 497–523 (2009).
- ⁴⁵J. J. Shepherd and A. Grüneis, "Many-body quantum chemistry for the electron gas: Convergent perturbative theories," *Phys. Rev. Lett.* **110**, 226401 (2013).
- ⁴⁶Y. Yang, V. Gorelov, C. Pierleoni, D. M. Ceperley, and M. Holzmann, "Electronic band gaps from quantum Monte Carlo methods," *Phys. Rev. B* **101**, 085115 (2020).
- ⁴⁷P. N. Keating, "Effect of invariance requirements on the elastic strain energy of crystals with application to the diamond structure," *Physical Review* **145**, 637–645 (1966).
- ⁴⁸L.-W. Wang and A. Zunger, "Solving Schrödinger's equation around a desired energy: Application to silicon quantum dots," *J. Chem. Phys.* **100**, 2394–2397 (1994).
- ⁴⁹A. Canning, L. Wang, A. Williamson, and A. Zunger, "Parallel empirical pseudopotential electronic structure calculations for million atom systems," *J. Comput. Phys.* **160**, 29–41 (2000).
- ⁵⁰J. E. Bernard and A. Zunger, "Electronic structure of ZnS, ZnSe, ZnTe, and their pseudobinary alloys," *Phys. Rev. B* **36**, 3199–3228 (1987).
- ⁵¹J. R. Chelikowsky and M. L. Cohen, "Nonlocal pseudopotential calculations for the electronic structure of eleven diamond and zinc-blende semiconductors," *Phys. Rev. B* **14**, 556–582 (1976).
- ⁵²G. Kresse and J. Hafner, "Ab initio molecular dynamics for liquid metals," *Phys. Rev. B* **47**, 558–561 (1993).
- ⁵³G. Kresse and J. Furthmüller, "Efficiency of ab-initio total energy calculations for metals and semiconductors using a plane-wave basis set," *Comput. Mater. Sci.* **6**, 15–50 (1996).
- ⁵⁴G. Kresse and J. Furthmüller, "Efficient iterative schemes for ab initio total-energy calculations using a plane-wave basis set," *Phys. Rev. B* **54**, 11169–11186 (1996).
- ⁵⁵G. Kresse and D. Joubert, "From ultrasoft pseudopotentials to the projector augmented-wave method," *Phys. Rev. B* **59**, 1758–1775 (1999).
- ⁵⁶P. E. Blochl, "Projector augmented-wave method," *Phys. Rev. B* **50**, 17953–17979 (1994).
- ⁵⁷J. P. Perdew, K. Burke, and M. Ernzerhof, "Generalized gradient approximation made simple," *Phys. Rev. Lett.* **77**, 3865–3868 (1996).
- ⁵⁸J. Heyd, G. E. Scuseria, and M. Ernzerhof, "Hybrid functionals based on a screened Coulomb potential," *J. Chem. Phys.* **118**, 8207–8215 (2003).
- ⁵⁹P. E. Blochl, O. Jepsen, and O. K. Andersen, "Improved tetrahedron method for Brillouin-zone integrations," *Phys. Rev. B* **49**, 16223–16233 (1994).
- ⁶⁰V. L. Deringer, A. L. Tchougréeff, and R. Dronskowski, "Crystal orbital Hamilton population (COHP) analysis as projected from plane-wave basis sets," *J. Phys. Chem. A* **115**, 5461–5466 (2011).
- ⁶¹R. Dronskowski and P. E. Blochl, "Crystal orbital Hamilton populations (COHP): Energy-resolved visualization of chemical bonding in solids based on density-functional calculations," *J. Phys. Chem.* **97**, 8617–8624 (1993).
- ⁶²S. Maintz, V. L. Deringer, A. L. Tchougréeff, and R. Dronskowski, "Analytic projection from plane-wave and PAW wavefunctions and application to chemical-bonding analysis in solids," *J. Comput. Chem.* **34**, 2557–2567 (2013).
- ⁶³S. Maintz, M. Esser, and R. Dronskowski, "Efficient rotation of local basis functions using real spherical harmonics," *Acta Physica Pol. B* **47**, 1165 (2016).
- ⁶⁴R. Nelson, C. Ertural, J. George, V. L. Deringer, G. Hautier, and R. Dronskowski, "LOBSTER: Local orbital projections, atomic charges, and chemical-bonding analysis from projector-augmented-wave-based density-functional theory," *J. Comput. Chem.* **41**, 1931–1940 (2020).
- ⁶⁵S. Maintz, V. L. Deringer, A. L. Tchougréeff, and R. Dronskowski, "LOBSTER: A tool to extract chemical bonding from plane-wave based DFT," *J. Comput. Chem.* **37**, 1030–1035 (2016).
- ⁶⁶M. Gajdoš, K. Hummer, G. Kresse, J. Furthmüller, and F. Bechstedt, "Linear optical properties in the projector-augmented wave methodology," *Phys. Rev. B* **73**, 045112 (2006).
- ⁶⁷M. Fox, *Optical Properties of Solids*, in *Oxford Master Series in Physics Condensed Matter Physics*, 2nd ed. (Oxford University Press, Oxford, 2012).
- ⁶⁸M. L. Cohen and V. Heine, "The fitting of pseudopotentials to experimental data and their subsequent application," *Solid State Phys.* **24**, 37–248 (1970).
- ⁶⁹J. Chelikowsky, D. J. Chadi, and M. L. Cohen, "Calculated valence-band densities of states and photoemission spectra of diamond and zinc-blende semiconductors," *Phys. Rev. B* **8**, 2786–2794 (1973).
- ⁷⁰J. L. Martins and M. L. Cohen, "Diagonalization of large matrices in pseudopotential band-structure calculations: Dual-space formalism," *Phys. Rev. B* **37**, 6134–6138 (1988).
- ⁷¹N. Troullier and J. L. Martins, "Efficient pseudopotentials for plane-wave calculations. II. Operators for fast iterative diagonalization," *Phys. Rev. B* **43**, 8861–8869 (1991).
- ⁷²M. R. Bonyadi and Z. Michalewicz, "Particle swarm optimization for single objective continuous space problems: A review," *Evol. Comput.* **25**, 1–54 (2017).
- ⁷³P. Paufler, "Landolt-Börnstein. Numerical data and functional relationships in science and technology. New series, editor in chief: K. H. Hellwege. Group III, crystal and solid state physics, Vol. 7, crystal structure data of inorganic compounds, W. Pies, A. Weiss, part b, key elements O, S, Se, Te, b3: Key elements S, Se, Te, Editors: K. H. Hellwege, A. M. Hellwege, Springer-Verlag Berlin 1982, XXVII, 435 Seiten. Leinen, Preis: DM 740,-," *Cryst. Res. Technol.* **18**, 1318 (1983).
- ⁷⁴J. D. H. J. D. H. Donnay and H. M. Ondik, *Crystal Data; Determinative Tables*, 3rd ed. (National Bureau of Standards, Washington, 1972/1973).
- ⁷⁵K. A. Mäder and A. Zunger, "Empirical atomic pseudopotentials for AlAs/GaAs superlattices, alloys, and nanostructures," *Phys. Rev. B* **50**, 17393–17405 (1994).
- ⁷⁶W. C. Swope, H. C. Andersen, P. H. Berens, and K. R. Wilson, "A computer simulation method for the calculation of equilibrium constants for the formation of physical clusters of molecules: Application to small water clusters," *J. Chem. Phys.* **76**, 637–649 (1982).
- ⁷⁷M. P. Teter, M. C. Payne, and D. C. Allan, "Solution of Schrödinger's equation for large systems," *Phys. Rev. B* **40**, 12255–12263 (1989).
- ⁷⁸A. V. Knyazev, "Toward the optimal preconditioned eigensolver: Locally optimal block preconditioned conjugate gradient method," *SIAM J. Sci. Comput.* **23**, 517–541 (2001).
- ⁷⁹A. V. Knyazev, M. E. Argentati, I. Lashuk, and E. E. Ovtchinnikov, "Block locally optimal preconditioned eigenvalue solvers (BLOPEX) in hypre and PETSc," *SIAM J. Sci. Comput.* **29**, 2224–2239 (2007).
- ⁸⁰J. R. Winkler, *Numerical Recipes In C: The Art Of Scientific Computing*, 2nd ed. (Endeavour, 1993), Vol. 17, pp. 201.
- ⁸¹S. Tomo, J. Langou, J. Dongarra, A. Canning, and L. Wang, "Conjugate-gradient eigenvalue solvers in computing electronic properties of nanostructure architectures," *Int. J. Comput. Sci. Eng.* **2**, 205 (2006).
- ⁸²J. Singh, *Physics of Semiconductors and Their Heterostructures* (McGraw-Hill, New York, 1993) oCLC: 221303860, International ed.
- ⁸³S. Shokhovets, O. Ambacher, and G. Gobsch, "Conduction-band dispersion relation and electron effective mass in III–V and II–VI zinc-blende semiconductors," *Phys. Rev. B* **76**, 125203 (2007).

- ⁸⁴ *Thin Film Solar Cells: Fabrication, Characterization and Applications*, 1st ed., edited by J. Poortmans and V. Arkhipov (Wiley, 2006).
- ⁸⁵ *Handbook of Photovoltaic Science and Engineering*, edited by A. Luque López and S. Hegedus (Wiley, Chichester, 2009) Repr ed.
- ⁸⁶ R. D. Paiva, R. A. Nogueira, C. D. Oliveira, H. W. L. Alves, J. L. A. Alves, L. M. R. Scolfaro, and J. R. Leite, "First-principles calculations of the effective mass parameters of $\text{Al}_x\text{Ga}_{1-x}\text{N}$ and $\text{Zn}_x\text{Cd}_{1-x}\text{Te}$ alloys," *Braz. J. Phys.* **32**, 405–408 (2002).
- ⁸⁷ C. Gueymard, D. Myers, and K. Emery, "Proposed reference irradiance spectra for solar energy systems testing," *Sol. Energy* **73**, 443–467 (2002).
- ⁸⁸ C. A. Gueymard, "The sun's total and spectral irradiance for solar energy applications and solar radiation models," *Sol. Energy* **76**, 423–453 (2004).
- ⁸⁹ K. Sato and S. Adachi, "Optical properties of ZnTe," *J. Appl. Phys.* **73**, 926–931 (1993).
- ⁹⁰ J. Rangel-Cárdenas and H. Sobral, "Optical absorption enhancement in CdTe thin films by microstructuring of the silicon substrate," *Materials* **10**, 607 (2017).
- ⁹¹ O. Center, Ohio Supercomputer Center (1987).
- ⁹² A. P. Thompson, H. M. Aktulga, R. Berger, D. S. Bolintineanu, W. M. Brown, P. S. Crozier, P. J. in't Veld, A. Kohlmeyer, S. G. Moore, T. D. Nguyen, R. Shan, M. J. Stevens, J. Tranchida, C. Trott, and S. J. Plimpton, "LAMMPS—A flexible simulation tool for particle-based materials modeling at the atomic, meso, and continuum scales," *Comput. Phys. Commun.* **271**, 108171 (2022).
- ⁹³ N. Ashcroft, "Electron-ion pseudopotentials in metals," *Phys. Lett.* **23**, 48–50 (1966).
- ⁹⁴ J. C. Kimball, R. W. Stark, and F. M. Mueller, "The Fermi surface of magnesium III: Local and nonlocal pseudopotential band structure models for magnesium," *Phys. Rev.* **162**, 600–608 (1967).